



High-Entropy Oxide Solar Selective Absorber

Yi-Cheng Lin¹ · Fitri Nur Indah Sari¹ · Siang-Yun Li¹ · Jyh-Ming Ting¹

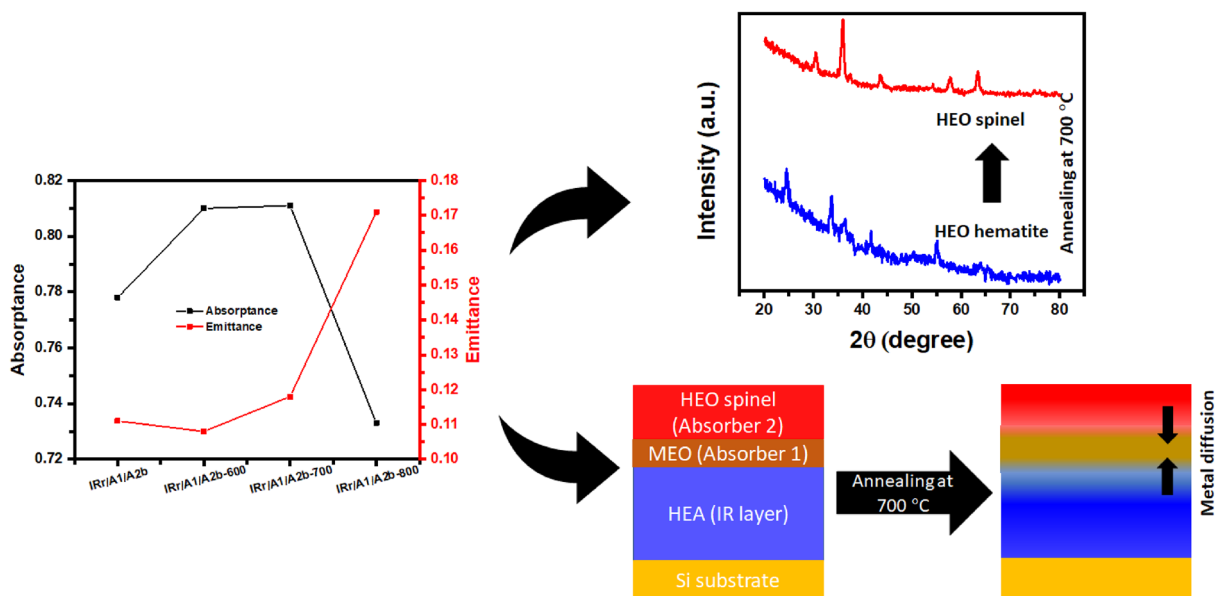
Received: 22 June 2023 / Accepted: 15 January 2024 / Published online: 21 February 2024
© The Author(s), under exclusive licence to Springer Science+Business Media, LLC 2024

Abstract

Sputter-deposited high-entropy materials, including high-entropy alloy (HEA) and high-entropy oxide (HEO), are demonstrated for use as selective solar absorber coatings (SSCs). Multi-layer SSC consists of CrFeCoNiAl HEA as the IR reflector layer, (CrFeCoNi)O medium-entropy oxide as the first layer absorber, and (CrMnFeCoNi)O HEO as the second layer absorber. The effects of phase and elemental concentration of the second layer absorber on the optical properties and thermal stability are addressed. The (CrMnFeCoNi)O HEO hematite has better spectral selectivity than the (CrMnFeCoNi)O HEO spinel. Meanwhile, from the X-Ray diffraction and transmission electron microscopy analyses of the annealed samples, the (CrMnFeCoNi)O HEO spinel exhibits better thermal stability than (CrMnFeCoNi)O HEO hematite. This work provides guidance to create an effective solar absorber.

Graphical Abstract

(CrMnFeCoNi)O hematite solar absorber exhibits better spectral selectivity than (CrMnFeCoNi)O spinel. (CrMnFeCoNi)O spinel exhibits better thermal stability than (CrMnFeCoNi)O hematite. The thermal instability of the spinel originates from the metal diffusion.



Keywords High-entropy oxide · Solar absorber coating · Spinel · Hematite · Thermal stability

✉ Jyh-Ming Ting
jting@mail.ncku.edu.tw

¹ Department of Materials Science and Engineering, National Cheng Kung University, Tainan 7010, Taiwan

Introduction

There are various green, renewable energy systems that convert the solar energy into electricity directly, such as solar photovoltaic cell [1], or indirectly, such as solar thermal power systems [2, 3]. One of the most promising solar thermal power systems is the concentrating solar power (CSP) system, involving the use of a solar selective absorber to convert the sunlight into thermal electric power. To maximize the efficiency, high absorptance (α) in the solar spectrum range and low thermal emittance (ε) in the infrared range (IR) are required. Depending on operation temperature, solar selective absorber can be grouped into low temperature ($T < 100$ °C), mid temperature (100 °C $< T < 450$ °C), and high-temperature ($T > 450$ °C) absorbers [4]. In the context of high-temperature solar selective absorber, Pyromark 2500, Ciemat, and spinel oxide-pigmented coatings are known as the state-of-the-art coatings. Pyromark 2500 is silicon-based paint that has high thermal stability up to 700 °C. However, the value of α starts to degrade at operating temperatures > 700 °C in air from 90 to 88% due to phase transformation and spallation [5, 6]. Multi-layer Ciemat coatings having Pt IR layer and two diffusion layers is also thermally stable up to 500 °C with α of 93% [7]. However, this coating degrades as the temperature increases to above 650 °C in air due to the degradation of Pt IR layer. Moreover, spinel oxide-pigmented coating exhibits a high thermal stability up to 750 °C with α of 93% [8].

Currently, high-temperature solar selective absorbers are being sought since a higher operation temperature leads to more thermal power to electricity conversion. Metal-dielectric composite or the so-called cermet is a conventional high-temperature solar selective absorber. A cermet consists of metal nanoparticles embedded in a dielectric matrix. For examples, Cr–Cr₂O₃ cermet is known as the black chrome [9]. To enhance solar absorption, a sandwiched structure consisting of an IR reflector in the bottom, a solar selective absorber in the middle, and an anti-reflective (AR) layer at the top is often used. In such a solar selective coating (SSC), the IR reflector reflects the thermal emission from the metallic substrate and the AR layer helps to enhance the light absorption. Moreover, the solar absorber itself is often multi-layered for improved solar absorption. High-temperature multi-layered SSCs include SS substrate/Cr IR reflector/low oxygen content Cr-AlO_x/mid-oxygen content Cr-AlO_x layer/high oxygen content Cr-AlO_x layer, giving $\alpha = 0.91$ and $\varepsilon = 0.225$ after annealing at 700 °C for 2 h in air [10], SS/TiN/alternating TiAlON and TiAlN layers, giving $\alpha = 0.788$ and $\varepsilon = 0.173$ after annealing at 600 °C for 50 h in air [11], SS/Mo/HfO_x/Mo/HfO₂, exhibiting absorption and emittance of 0.874 and 0.15, respectively, after annealing at 525 °C in air [12].

In the past few years, a new class of materials, namely, high-entropy materials, has emerged at the center stage of materials research, thanks to the discovery of high-entropy alloy in 2004 [13] and the report of high-entropy oxide (HEO) in 2015 [14]. HEMs have been shown to exhibit a number of excellent characteristics. High-temperature structural stability between 850 and 1000 °C has been demonstrated in, for example, (MgCoNiCuZn)O [14] and between 450 and 850 °C in, for example, (CoCrFeMnNi)₃O₄ [15]. (Yb_{0.2}Y_{0.2}Lu_{0.2}Sc_{0.2}Gd_{0.2})₂Si₂O₇ has good corrosion resistance in water–vapor environment and displays excellent phase stability from room temperature to 1300 °C [16]. (Mg_{0.2}Co_{0.2}Ni_{0.2}Cu_{0.2}Zn_{0.2})O, (Li, Mg, Co, Ni, Cu, Zn)O, and (Zn, Fe, Ni, Mg, Cd)Fe₂O₄ have been shown to exhibit huge dielectric constants [17, 18]. Along with the demonstration of these characteristics, HEOs have been prepared using methods, such as solid-state reaction [14, 19], hydrothermal synthesis [20, 21], solvothermal synthesis [22], solution combustion synthesis [15], nebulized spray pyrolysis [23], and reverse co-precipitation [24]. The resulting materials are powders or nanoparticles. It appears that there are and only limited studies reported thin-film HEOs obtained using a PVD process [25]. In the meantime, in the past few years, there are several works on high-entropy materials for solar absorber material, including AlCrTaTiZrN [26], MoNbHfZrTi [27], HfNbTaTiZrN [28], MoNbHfZrTi [29], AlMo_{0.5}NbTa_{0.5}TiZrN_x [30], and HEO, has been demonstrated for solar absorber. It is seen that almost no study demonstrate the use of HEO for solar absorber coating.

In this work, we have explored the use of sputter-deposited HEAs and HEOs for use SSCs. The IR reflector layer is a CrFeCoNiAl HEA, and the multi-layered absorber consists of a medium-entropy oxide (MEO) of (CrFeCoNi)O and HEO of (CrMnFeCoNi)O. Relation among the composition, structure, and optical property is investigated. The resulting SSCs have also been evaluated for the thermal stability. In the meantime, we have also investigated the effect of two different HEO crystal structures, e.g., HEO spinel and hematite, for the degradation mechanisms. This work provides a guidance for optimizing oxide material for high-temperature solar absorber coating.

Experimental

CrFeCoNiAl HEA, (CrFeCoNi)O MEO, and (CrMnFeCoNi)O HEO were deposited on (100) Si and 316L SS substrates using a RF co-sputtered deposition method. The target-to-substrate distance was fixed at 130 mm and the deposition chamber was evacuated to lower than 5×10^{-6} Torr and then back filled with 20-sccm Ar before the deposition. The working pressure was 5×10^{-3} torr and the substrate was rotated at 5 rpm. High-purity (99.99%)

Ar and O₂ gasses were used as working gas and reactive gas, respectively. For the CrFeCoNiAl IR reflector (designated as IRr), an Al target (99.995%) and a composite target of Cr, Fe, Co, Ni (99.995%) were used. The RF powers for the Al and composite targets were 80 and 120 W, respectively. For the first absorber layer of (CrFeCoNi)O MEO (designated as A1), the composite target was used. The power was 100 W and O₂/Ar = 2 sccm/20 sccm. Manganese oxide (MnO) target (99.995%) and the composite target were used to deposit the second absorber layer of (CrMnFeCoNi)O HEO. Two such HEOs were made. One was obtained at a MnO target power of 100 W, (CrFeCoNi) alloy target power of 80 W, and O₂/Ar = 2 sccm/20 sccm, giving sample A2a. The other was obtained at a MnO target power of 80 W, (CrFeCoNi) alloy target power of 100 W, and O₂/Ar = 7 sccm/20 sccm, giving sample A2b. The substrate was externally heated at 800 °C for the deposition of all oxides. In contrast, no external heating was applied to the substrate for the deposition of the HEA. A matrix summarizing the deposition conditions is given in Table S1 in the Supporting Information. For the thermal stability test, as-deposited samples were post-annealed in air at different temperatures of 600, 700, and 800 °C for 2 h (heating rate = 6.67 °C/min).

The thickness of coating was determined using profilometer and field emission scanning electron microscopy (SEM, JOEL6701). The chemical composition was examined using Energy-dispersive X-ray spectroscopy (EDS, JOEL6701). The refractive index and extinction coefficient were investigated using ellipsometer (J.A. Woollam /M2000-DI). The crystal structure was studied using glazing angle X-ray diffraction (GIXRD, Bruker D8-Discover). The reflectance from 300 to 2500 nm wavelength was measured using UV/Vis/NIR spectrophotometry equipped with an integrated sphere (LAMBDA TM 950, PerkinElmer). The solar absorptance (α) was calculated as follows using Eq. (1) [31], where E_s is the intensity of incident solar light, A is the absorbance, and R is the reflectance.

$$\alpha = \frac{\int_{300}^{2500} E_s(\lambda)A(\lambda)d\lambda}{\int_{300}^{2500} E_s(\lambda)d\lambda} = \frac{\int_{300}^{2500} E_s(\lambda)[1 - R(\lambda)]d\lambda}{\int_{300}^{2500} E_s(\lambda)d\lambda}. \quad (1)$$

Emission was measured using Emissionmetry (Emissionmeter K3, Optosol GmbH). It consists of an integrating sphere, glow bars as the sources of thermal radiation, and 3 detectors, which are sensitive for 3.9-, 5.1-, and 10- μ m wavelengths. Emissionmetry gave thermal emittance (ϵ) at room temperature that at 100 °C was calculated. Thermal emittance was calculated as follows using Eq. (2) [31], where $E_{100^\circ\text{C}}$ is the black body radiation at 100 °C.

$$\epsilon = \frac{\int_{2500}^{10000} A(\lambda)E_{100^\circ\text{C}}(\lambda)d\lambda}{\int_{2500}^{10000} E_{100^\circ\text{C}}(\lambda)d\lambda}. \quad (2)$$

The structure properties of the annealed coatings were investigated using GIXRD and transmission electron microscopy (HR-TEM, JEOL JEM-2100F).

Results and Discussion

SEM analysis shows that the surface morphology of the HEA IRr is granular (Fig. 1a). Similar surface morphology was found for the MEO and HEO absorber layers, as shown in Fig. 1b for HEO. From the cross-section, it is seen that all layers have columnar structure, which is typical structure obtained using sputter deposition. This morphology with surface texture is beneficial for light absorption, thus increasing solar absorption and thermal ability [32]. All the coating thicknesses are very uniform, as shown in Fig. 1c and d for the IRr and A1 layers, respectively. The HEA IRr has a BCC structure (JCPDF #47-1126) [33], as shown in Fig. 2. EDS analysis shows that the composition of the HEA is Cr/Fe/Co/Ni/Al = 10.7/25.1/6.0/5.1/23.2 in at %. The A1 MEO layer is a spinel oxide (JCPDF #73-1856), having Cr/Fe/Co/Ni = 9.7/9.8/12.8/67.7 in at %. The A2a HEO also has a spinel structure (JCPDF #84-0482). Meanwhile, the A2b HEO has a hematite structure (JCPDF #84-0311). The chemical compositions of A2a and A2b are Cr/Mn/Fe/Co/Ni = 4.6/47.1/5.2/7.9/35.3 and 8.5/25.5/7.1/11/47.9, respectively. The different chemical compositions in the A2a and A2b are due to the different power used for the MnO and CrFeCoNi composite. Sputtering power is related to the kinetic energy of the target atoms. A higher sputtering power results in higher surface diffusions once these atoms are adsorbed on the substrate surface [34]. As a result, A2a has larger amount of Mn than that of A2b layer. This is due to A2a was deposited at higher sputtering power of 100 W, while A2b was deposited at smaller sputtering power of 80 W. Likewise, the Cr, Fe, Co, and Ni concentrations are higher in A2b layer due to its higher sputtering powers of CrFeCoNi target.

The reflective indexes of these single layers are first presented. The reflective indexes at 500 nm of the single layers are 3.50, 2.62, 2.35, and 2.32 for IRr, A1, A2a, and A2b, respectively (Fig. 3 and Table S1). The reflective index gradually decreases from the IRr to A1 and then to A2. Meanwhile, the extinction coefficient at 500 nm of the single layers are 2.78, 0.6, 0.62, and 0.86 for IRr, A1, A2a, and A2b, respectively. As a result, SSCs consisting of IRr/A1/A2a and IRr/A1/A2b various layers are examined. Figure 4a shows the reflectance spectra of various single and multi-layer SSCs. The addition of layers gives low reflectance in

Fig. 1 SEM top views of **a** IRr and **b** A2b layers. SEM cross-sectional views of **c** IRr and **d** A1 on Si substrate

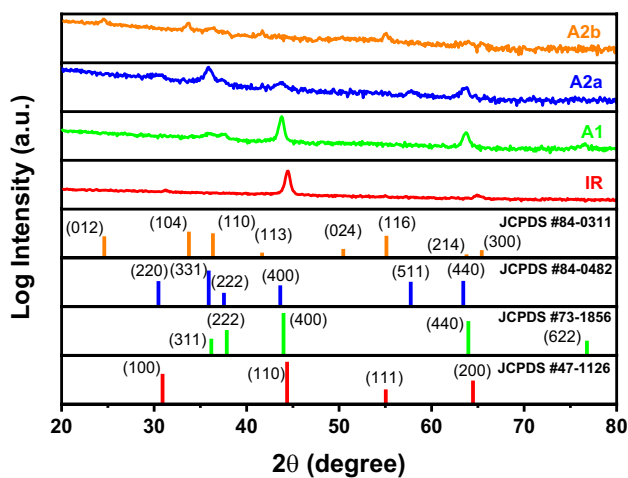
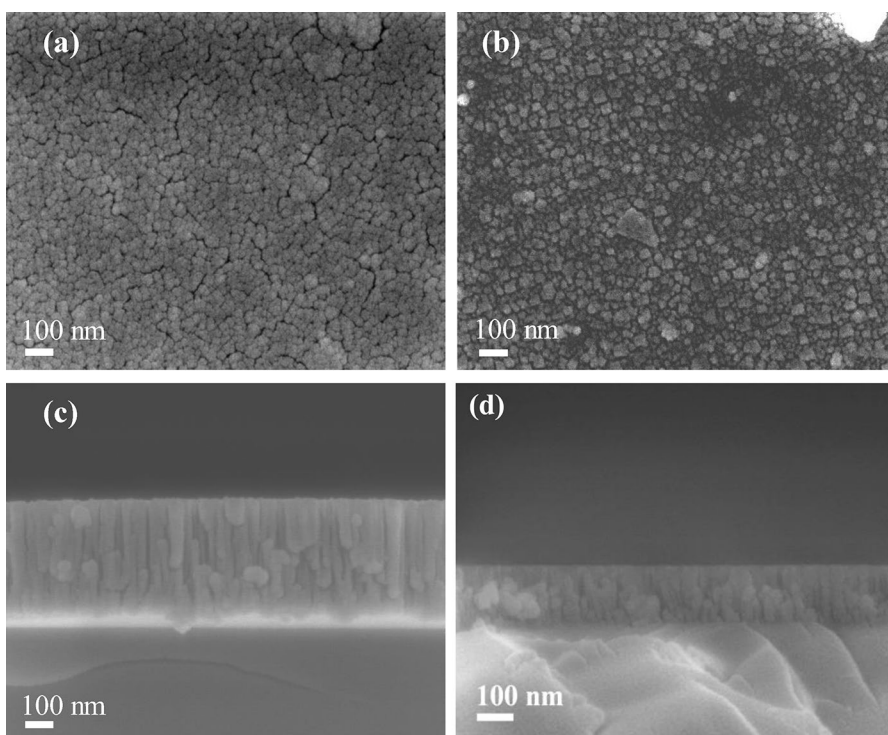


Fig. 2 GIXRD patterns of as-deposited coatings on Si substrate

the solar spectrum, indicating higher α . Comparing the IRr/A1/A2a and IRr/A1/A2b, the IRr/A1/A2a has slightly better α of 0.81 vs 0.78, as shown in Fig. 4b. However, the ϵ of the IRr/A1/A2b is slightly smaller than IRr/A1/A2a, 0.111 vs 0.130. Spectral selectivity (α/ϵ) of both multilayer SSCs is thus determined. The IRr/A1/A2b has α/ϵ of 7, which is higher than that of IRr/A1/A2a (6.2). To understand the better performance of the IRr/A1/A2b, the reflectance spectra of single layers A2a and A2b were obtained, as shown in Figure S1. The single layer A2b exhibits higher α/ϵ of 6.6, compared to that of A2a (6). Moreover, the absorption of

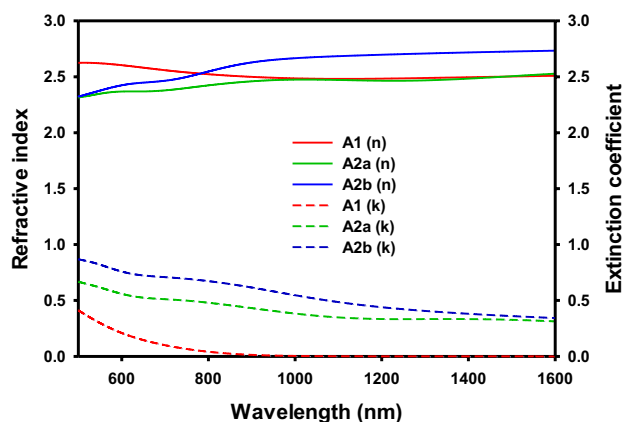


Fig. 3 Reflective index and extinction coefficient of as-deposited coatings on Si substrate

the thin film occurs due to two mechanisms, one is intrinsic absorption, which is characterized by the extinction coefficient of the film and the other one is interference-induced absorption. The A2b has a higher extinction coefficient of 0.86 than A2a (0.6), indicating its higher absorption capability.

The thermal stability of the SSCs was thus investigated at different temperatures of 600, 700, and 800 °C for 2 h in air. Figure 5 shows that the solar absorptance and emittance of IRr/A1/A2a coating remain the same at 600 °C. The decrement of spectral selectivity is observed with the rising temperature. On the other hand, IRr/A1/A2b coating

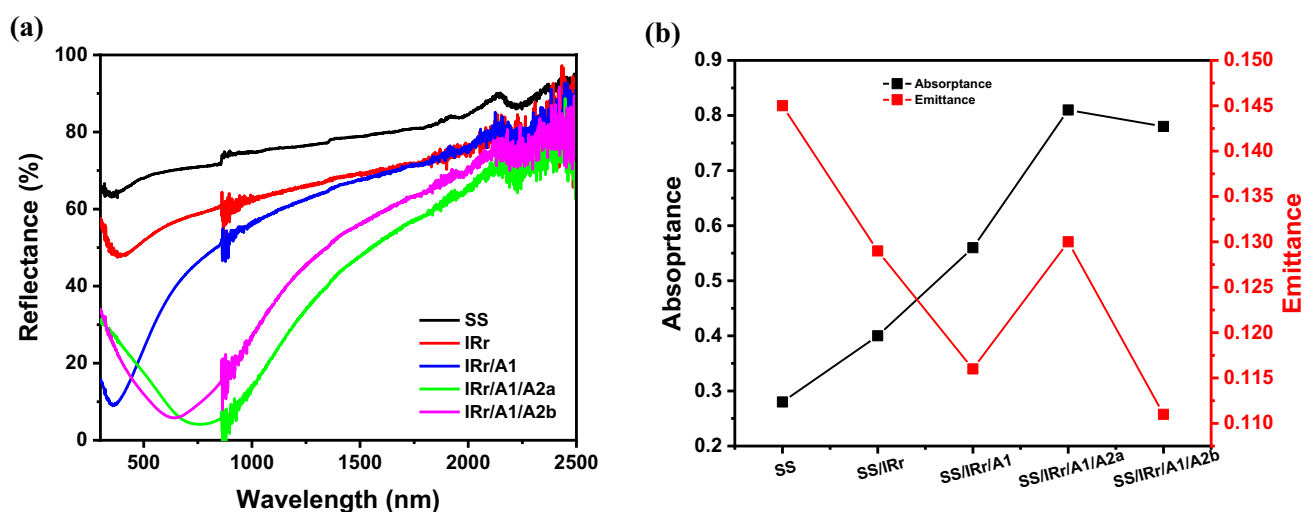


Fig. 4 a Reflectance spectra and b solar absorbance and emittance of as-deposited single and multiple layer coatings on SS substrate

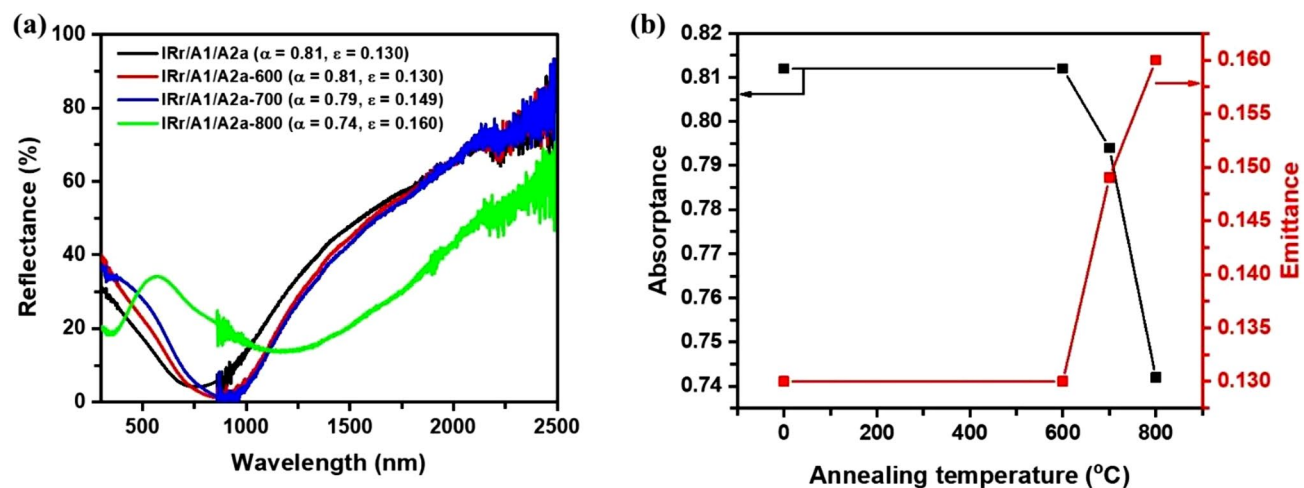


Fig. 5 a Reflection spectra and b absorbance and emittance of as-deposited IRr/A1/A2a SSC on SS substrate and post-annealing at 600, 700, and 800 °C in air

exhibits a higher solar absorbance and smaller emittance at 600 °C (Fig. 6). The spectral selectivity decreases at a higher temperature of 700 °C and significantly decreases at 800 °C.

The SSCs show optical degradation after annealing at ≥ 700 °C. Various post-analysis was performed to understand the phase, morphology, and elemental changing after annealing treatment. XRD analysis was first performed on the post-annealing A2a and A2b coating layers to understand the phase stability after annealing. The crystal structure of the A2a after post-annealing at 600 and 700 °C remains the same as before annealing, which is spinel oxide (Fig. 7a). This indicates the structural stability of A2a. It was reported that the HEO spinel has high thermal stability due to its small chemical diffusion coefficient at low-pressure oxygen (high temperature) [35, 36].

Meanwhile, A2b shows crystalline structure changes with the annealing temperature. The structure transforms from hematite for as-synthesized coating to spinel oxide for coating after post-annealing at 600 and 700 °C, as shown in Fig. 7b. Furthermore, the crystallinity of the spinel oxide becomes better with increasing temperature. Thus, the phase transformation in A2b accounts for thermal degradation. Moreover, the result also confirms that spinel oxide has better phase stability than hematite oxide. Due to there is no phase transformation in the A2a, the post-TEM analysis was performed on IRr/A1/A2a-700 to further investigate the root cause of the degradation. It was found that the thickness of the A1 layer of IRr/A1/A2a-700 was wider as compared to the as-deposited IRr/A1/A2a, 25.1 vs 8.4 nm (Fig. 8). On the other hand, the thickness of the

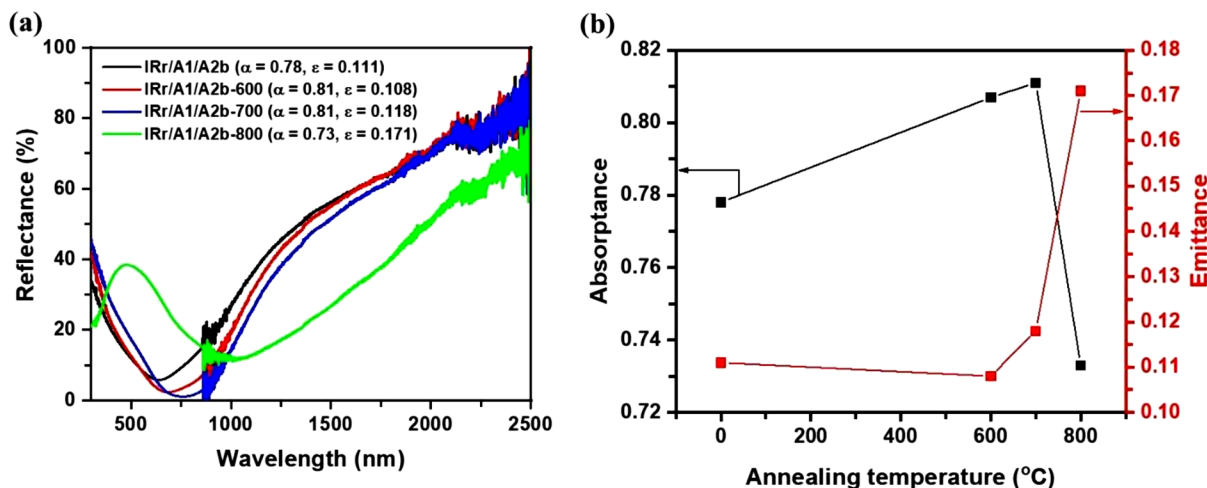


Fig. 6 a Reflectance spectra and b absorbance and emittance of as-deposited IRr/A1/A2b SSC on SS substrate and post-annealing at 600, 700, and 800 °C in air

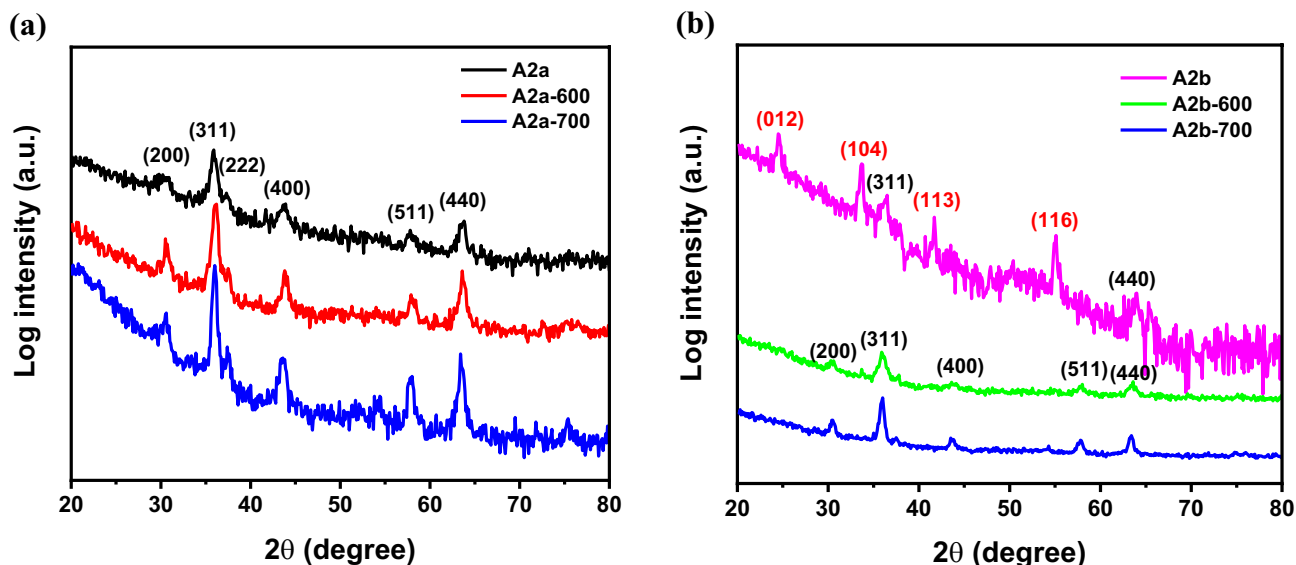


Fig. 7 XRD patterns of as-deposited SSC and post-annealing at 600 and 700 °C in air for 2 h on SS substrate

A2a layer after annealing at 700 °C becomes shrinkage. EDS analysis was performed to understand the elemental concentration change due to diffusion at high temperature. It is seen that A2a and IR layers show insignificant change after annealing at 700 °C. Meanwhile, the A1 layer shows significant change in elemental composition after annealing at 700 °C. Almost all of the metal concentration decreases after annealing at 700 °C, except Al, as shown in Table 1. The reduction of the Cr, Mn, Fe, Co, and Ni concentration in the A1 layer of IRr/A1/A2a might be due to the diffusion into either IRr or A2a layers. It is noted that the Al concentration in A1 significantly increases after

annealing at 700 °C, from 9.6 to 31.7%. This indicates the diffusion of the Al from the IRr layer toward A1. This can be explained since the melting point of Al is 660 °C, thus annealing at 700 °C triggers its diffusion. The diffusion of Al also can be seen from EDS mapping (Figures S2 and S3). Furthermore, after annealing, it is obvious that the Cr in the IRr layer is not uniformly distributed, forming aggregation. From the post-XRD, -TEM, and -EDS analyses, the degradation of the spectral selectivity of the IRr/A1/A2a is due to the chemical structural instability in the A1 layer and aggregation of Cr in the IRr layer.

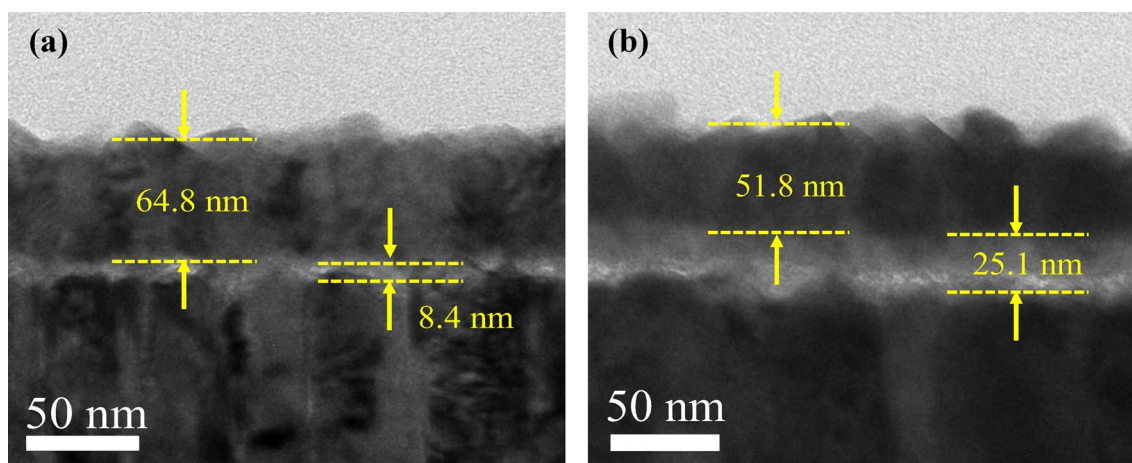


Fig. 8 TEM images of **a** as-deposited IRr/A1/A2a and **b** IRr/A1/A2a after post-annealing at 700 °C in air for 2 h on SS substrate

Table 1 EDS point analysis of A1 layers

Element	IRr		A1		A2a	
	As-deposited	Post-annealing 700 °C)	As-deposited	Post-annealing 700 °C)	As-deposited	Post-annealing 700 °C)
O	–	5.38	45.16	51.83	46.29	45.94
Al	28.68	27.33	9.58	31.68	0.25	1.35
Cr	15.67	12.56	11.44	8.06	3.69	3.14
Mn	–	0.09	2.28	1.78	13.91	11.53
Fe	10.92	10.78	4.72	0.87	3.72	4.21
Co	18.11	17.43	10.38	1.29	10.92	12.82
Ni	26.63	26.42	16.45	4.48	21.22	21.02

Conclusion

In this work, sputter-deposited high-entropy materials were demonstrated for use as SSCs. Multi-layer SSC consists of CrFeCoNiAl HEA as the IR reflector layer, (CrFeCoNi)O MEO as the first layer absorber, and (CrMnFeCoNi)O HEO as the second layer absorber. The multi-layered structure enhances the solar absorptance and reduces the emission. Moreover, the phase and elemental concentration of the second absorber layer affect the spectral selectivity and thermal stability. The (CrMnFeCoNi)O HEO hematite has better spectral selectivity than (CrMnFeCoNi)O HEO spinel due to its higher extinction coefficient. Meanwhile, the (CrMnFeCoNi)O HEO spinel exhibits better thermal stability than (CrMnFeCoNi)O HEO hematite due to its phase and structural stability.

Supplementary Information The online version contains supplementary material available at <https://doi.org/10.1007/s44210-024-00028-0>.

Acknowledgements This work was supported by the National Science and Technology Council under Grant Number NSTC 112-2224-E-006-003.

Data Availability Data are available on request.

Declarations

Conflict of interest On behalf of all authors, the corresponding author states that there is no conflict of interest.

References

1. M.A. Green, K. Emery, Y. Hishikawa, W. Warta, E.D. Dunlop, Solar cell efficiency tables (Version 45). *Prog. Photovolt. Res. Appl.* **23**, 1–9 (2015)
2. D. Abbott, Keeping the energy debate clean: how do we supply the world's energy needs? *Proc. IEEE* **98**, 42–66 (2009)
3. N.S. Lewis, G. Crabtree, A.J. Nozik, M.R. Wasielewski, P. Alivisatos, H. Kung, J. Tsao, E. Chandler, W. Walukiewicz, M. Spitzer, Basic Research Needs for Solar Energy Utilization. Report of the Basic Energy Sciences Workshop on Solar Energy Utilization, April 18–21, 2005. DOESC (USDOE Office of Science (SC)), (2005)
4. C.E. Kennedy, Review of mid- to high-temperature solar selective absorber materials. National Renewable Energy Laboratory (2002). <https://doi.org/10.2172/15000706>
5. C.K. Ho, A.R. Mahoney, A. Ambrosini, M. Bencomo, A. Hall, T.N. Lambert, Characterization of pyromark 2500 paint for

- high-temperature solar receivers. *J. Sol. Energy Eng.* (2013). <https://doi.org/10.1115/1.4024031>
6. S. Hosseini, J.F. Torres, M. Taheri, A. Tricoli, W. Lipiński, J. Coventry, Long-term thermal stability and failure mechanisms of Pyromark 2500 for high-temperature solar thermal receivers. *Sol. Energy Mater. Sol. Cells* **246**, 111898 (2022)
 7. J. Liu, Thermodynamically stable, plasmonic transition metal oxide nanoparticle solar selective absorbers towards 95% optical-to-thermal conversion efficiency at 750 °C. National Renewable Energy Laboratory (2021). <https://doi.org/10.2172/1890656>
 8. X. Wang, E. Lee, C. Xu, J. Liu, High-efficiency, air-stable manganese–iron oxide nanoparticle-pigmented solar selective absorber coatings toward concentrating solar power systems operating at 750 °C. *Mater. Today Energy* **19**, 100609 (2021)
 9. Y. Yin, Y. Pan, L. Hang, D. McKenzie, M. Bilek, Direct current reactive sputtering Cr–Cr₂O₃ cermet solar selective surfaces for solar hot water applications. *Thin Solid Films* **517**, 1601–1606 (2009)
 10. H. Liu, Q. Wan, B. Lin, L. Wang, X. Yang, R. Wang, D. Gong, Y. Wang, F. Ren, Y. Chen, The spectral properties and thermal stability of CrAlO-based solar selective absorbing nanocomposite coating. *Sol. Energy Mater. Sol. Cells* **122**, 226–232 (2014)
 11. H. Liu, B. Yang, M. Mao, Y. Liu, Y. Chen, Y. Cai, D. Fu, F. Ren, Q. Wan, X. Hu, Enhanced thermal stability of solar selective absorber based on nano-multilayered TiAlON films deposited by cathodic arc evaporation. *Appl. Surf. Sci.* **501**, 144025 (2020)
 12. N. Selvakumar, H.C. Barshilia, K. Rajam, A. Biswas, Structure, optical properties and thermal stability of pulsed sputter deposited high temperature HfO_x/Mo/HfO₂ solar selective absorbers. *Sol. Energy Mater. Sol. Cells* **94**, 1412–1420 (2010)
 13. M.-H. Tsai, J.-W. Yeh, High-entropy alloys: a critical review. *Mater. Res. Lett.* **2**, 107–123 (2014)
 14. C.M. Rost, E. Sacht, T. Borman, A. Moballeghe, E.C. Dickey, D. Hou, J.L. Jones, S. Curtarolo, J.-P. Maria, Entropy-stabilized oxides. *Nat. Commun.* **6**, 8485 (2015)
 15. A. Mao, F. Quan, H.-Z. Xiang, Z.-G. Zhang, K. Kuramoto, A.-L. Xia, Facile synthesis and ferrimagnetic property of spinel (CoCrFeMnNi)₃O₄ high-entropy oxide nanocrystalline powder. *J. Mol. Struct.* **1194**, 11–18 (2019)
 16. Y. Dong, K. Ren, Y. Lu, Q. Wang, J. Liu, Y. Wang, High-entropy environmental barrier coating for the ceramic matrix composites. *J. Eur. Ceram. Soc.* **39**, 2574–2579 (2019)
 17. D. Bérardan, S. Franger, D. Dragoe, A.K. Meena, N. Dragoe, Colossal dielectric constant in high entropy oxides. *Phys. Status Solidi RRL* **10**, 328–333 (2016)
 18. A. Radoń, Ł. Hawelek, D. Łukowiec, J. Kubacki, P. Włodarczyk, Dielectric and electromagnetic interference shielding properties of high entropy (Zn, Fe, Ni, Mg, Cd) Fe₂O₄ ferrite. *Sci. Rep.* **9**, 1–13 (2019)
 19. J. Dąbrowa, M. Stygar, A. Miśka, A. Knapik, K. Mroccka, W. Tejchman, M. Danielewski, M. Martin, Synthesis and microstructure of the (Co, Cr, Fe, Mn, Ni)₃O₄ high entropy oxide characterized by spinel structure. *Mater. Lett.* **216**, 32–36 (2018)
 20. M. Biesuz, L. Spiridigliozzi, G. Dell’Agli, M. Bortolotti, V.M. Sglavo, Synthesis and sintering of (Mg, Co, Ni, Cu, Zn) O entropy-stabilized oxides obtained by wet chemical methods. *J. Mater. Sci.* **53**, 8074–8085 (2018)
 21. L. Spiridigliozzi, C. Ferone, R. Cioffi, G. Accardo, D. Frattini, G. Dell’Agli, Entropy-stabilized oxides owning fluorite structure obtained by hydrothermal treatment. *Materials* **13**, 558 (2020)
 22. D. Wang, Z. Liu, S. Du, Y. Zhang, H. Li, Z. Xiao, W. Chen, R. Chen, Y. Wang, Y. Zou, Low-temperature synthesis of small-sized high-entropy oxides for water oxidation. *J. Mater. Chem. A* **7**, 24211–24216 (2019)
 23. A. Sarkar, L. Velasco, D. Wang, Q. Wang, G. Talasila, L. de Biasi, C. Kübel, T. Brezesinski, S.S. Bhattacharya, H. Hahn, High entropy oxides for reversible energy storage. *Nat. Commun.* **9**, 1–9 (2018)
 24. A. Sarkar, R. Djenadic, N.J. Usharani, K.P. Sanghvi, V.S. Chakravadhanula, A.S. Gandhi, H. Hahn, S.S. Bhattacharya, Nanocrystalline multicomponent entropy stabilised transition metal oxides. *J. Eur. Ceram. Soc.* **37**, 747–754 (2017)
 25. P. Meisenheimer, T. Kratočil, J. Heron, Giant enhancement of exchange coupling in entropy-stabilized oxide heterostructures. *Sci. Rep.* **7**, 1–6 (2017)
 26. C.-Y. He, X.-H. Gao, D.-M. Yu, X.-L. Qiu, H.-X. Guo, G. Liu, Scalable and highly efficient high temperature solar absorber coatings based on high entropy alloy nitride AlCrTaTiZrN with different antireflection layers. *J. Mater. Chem. A* **9**, 6413–6422 (2021)
 27. C.-Y. He, X.-H. Gao, M. Dong, X.-L. Qiu, J.-H. An, H.-X. Guo, G. Liu, Further investigation of a novel high entropy alloy MoNbHfZrTi based solar absorber coating with double antireflective layers. *Solar Energy Mater. Solar Cells* **217**, 110709 (2020)
 28. C.-Y. He, X.-H. Gao, D.-M. Yu, S.-S. Zhao, H.-X. Guo, G. Liu, Toward high-temperature thermal tolerance in solar selective absorber coatings: choosing high entropy ceramic HfNbTaTiZrN. *J. Mater. Chem. A* **9**, 21270–21280 (2021)
 29. H.-X. Guo, C.-Y. He, X.-L. Qiu, Y.-Q. Shen, G. Liu, X.-H. Gao, A novel multilayer high temperature colored solar absorber coating based on high-entropy alloy MoNbHfZrTi: optimized preparation and chromaticity investigation. *Solar Energy Mater. Solar Cells* **209**, 110444 (2020)
 30. S.-S. Zhao, C.-Y. He, X.-L. Qiu, P. Zhao, B.-H. Liu, G. Liu, X.-H. Gao, G.-K. Tian, High-entropy alloy nitride AlMo_{0.5}NbTa_{0.5}TiZrN_x-based high-temperature solar absorber coating: structure, optical properties, and thermal stability. *ACS Appl. Energy Mater.* **5**, 9214–9224 (2022)
 31. M. López-Herraiz, A.B. Fernández, N. Martínez, M. Gallas, Effect of the optical properties of the coating of a concentrated solar power central receiver on its thermal efficiency. *Sol. Energy Mater. Sol. Cells* **159**, 66–72 (2017)
 32. X.-H. Gao, X.-L. Qiu, X.-T. Li, W. Theiss, B.-H. Chen, H.-X. Guo, T.-H. Zhou, G. Liu, Structure, thermal stability and optical simulation of ZrB₂ based spectrally selective solar absorber coatings. *Solar Energy Mater. Sol. Cells* **193**, 178–183 (2019)
 33. J.W. Yeh, S.K. Chen, S.J. Lin, J.Y. Gan, T.S. Chin, T.T. Shun, C.H. Tsau, S.Y. Chang, Nanostructured high-entropy alloys with multiple principal elements: novel alloy design concepts and outcomes. *Adv. Eng. Mater.* **6**, 299–303 (2004)
 34. K. Srinivas, M. Manivel Raja, D.V. Sridhara Rao, S.V. Kamat, Effect of sputtering pressure and power on composition, surface roughness, microstructure and magnetic properties of as-deposited Co₂FeSi thin films. *Thin Solid Films* **558**, 349–355 (2014)
 35. Y. He, L. Zhang, H.W. Xiong, K.C. Zhou, X. Kang, The selective site occupation, structural and thermal stability of high entropy (CoCrFeMnNi)₃O₄ spinel. *J. Alloys Comp.* **965**, 171428 (2023)
 36. Z. Grzesik, G. Smoła, M. Miszczak, M. Stygar, J. Dąbrowa, M. Zajusz, K. Świerczek, M. Danielewski, Defect structure and transport properties of (Co, Cr, Fe, Mn, Ni)₃O₄ spinel-structured high entropy oxide. *J. Eur. Ceram. Soc.* **40**, 835–839 (2020)

Publisher’s Note Springer Nature remains neutral with regard to jurisdictional claims in published maps and institutional affiliations.

Springer Nature or its licensor (e.g. a society or other partner) holds exclusive rights to this article under a publishing agreement with the author(s) or other rightsholder(s); author self-archiving of the accepted manuscript version of this article is solely governed by the terms of such publishing agreement and applicable law.